Chemical Engineering Journal 505 (2025) 159380

Contents lists available at ScienceDirect

Chemical Engineering Journal

journal homepage: www.elsevier.com/locate/cej

Butterfly-shaped dendrimers with photosensitizer recruitment function for enhanced light-controlled precise cascaded ROS and NO release in multimodal diabetic foot ulcers infections treatment

Xiangyu Huang [a,1], Zucheng Shen [a,1], Qi Deng [a,1], Chengfei Zhao [b], Xiaofeng Cai [a], Shaoteng Huang [a], Mingbo Zhang [a], Yanzhuo Lv [a], Dongliang Yang [c,*], Junyang Zhuang [a,*], Ning Li [a,*]

[a] Fujian Key Laboratory of Drug Target Discovery and Structural and Functional Research, School of Pharmacy, Fujian Medical University, Fuzhou 350122 PR China
[b] Department of Pharmacy, School of Pharmacy and Medical Technology, Putian University, Putian 351100 PR China
[c] Key Laboratory of Flexible Electronics (KLOFE) and Institute of Advanced Materials (IAM), School of Physical and Mathematical Sciences, Nanjing Tech University (NanjingTech), Nanjing 211800 PR China

ARTICLE INFO

Keywords:
Amphiphilic peptide dendrimers
Cascade amplification
Gas therapy
Photodynamic therapy
Diabetic foot ulcer infection
Biofilm

ABSTRACT

Diabetic foot ulcers (DFU) infections have been a major setback in wound healing, yet there is no effective therapeutic intervention. Here we report a nano-multidrug co-delivery system based on arginine-terminal butterfly-shaped peptide dendrimers (C&D@Z) that effectively kill bacteria and promote wound healing. Firstly, upon the near-infrared light irradiation, reactive oxygen species (ROS) was generated from the loaded photosensitizers, and then mediated bacteria killing. Next, the excessive ROS reacted with the designed butterfly-shaped dendrimers to generate sustained and abundant nitric oxide (NO), which exerted bactericidal action, as well as produced anti-inflammatory and angiogenesis effects. The co-delivery system, facilitated by the generation of NO, penetrated deeply into the biofilm, thereby effectively eliminating bacteria. The enhanced bactericidal and healing efficiency was investigated through biofilm penetration and wound healing experiments. Collectively, our system leveraged the highly-branched and cavity structures of the butterfly peptide dendrimer to realize the tight contact between the arginine groups and photosensitizer to achieve efficient conversion from ROS to NO, and the C&D@Z exhibited superior NO production, optimal photodynamic therapy utilization and effective penetration performance through cascade reaction between photodynamic therapy and NO therapy, may serve as a promising therapeutic approach for DFU infections.

1. Introduction

Diabetes is a chronic metabolic disease characterized by hyperglycemia and one of the leading causes of disability or even death [1]. The Diabetic Foot Ulcer (DFU), the most representative and critical complication of diabetes [2], arises from elevated blood glucose-induced vascular lesions and neuropathy in the feet [3], compounded by reduced blood flow, inadequate blood supply and abnormal sensation [4], collectively increasing the risk of DFU occurrence. Furthermore, diabetic wounds are vulnerable to bacteria and induce stalled healing due to the damage of blood vessels and exposed wounds [5], while persistent inflammation from infection significantly hinders the healing process and can potentially lead to limb amputation [6]. Therefore, there is an urgent need for innovative treatment strategies to address this issue in the management of diabetic wound infections [7,8]. In diabetic wounds, elevated blood glucose levels promote bacterial growth and biofilm formation [9]. These biofilms possess the characteristics of low pH, high Glutathione (GSH), high H_2O_2, high oxidative stress levels, and hypoxia [10] because of the protection of extracellular polymeric substances (EPS) [11] that distinguish biofilms from planktonic bacteria [12,13]. The EPS serves as a protective barrier that not only protects the bacterial inhabitants from the host's innate immune cells, but also prevents the penetration of antimicrobial agents [14]. Clinically, administration of high-dose antibiotics is often the primary

* Corresponding authors.
E-mail addresses: yangdl1023@njtech.edu.cn (D. Yang), jyzhuang@fjmu.edu.cn (J. Zhuang), ningli@fjmu.edu.cn (N. Li).
[1] These authors contributed equally to this work.

https://doi.org/10.1016/j.cej.2025.159380
Received 5 November 2024; Received in revised form 7 December 2024; Accepted 6 January 2025
Available online 7 January 2025

treatment for bacterial biofilm-associated infections [15,16]. However, these treatments are not only susceptible to drug resistance, but also cause a wide range of side effects, causing pain and heavy burden on patients [17]. Therefore, it is imperative to develop alternative strategies that combine antibiotic-free antimicrobial methods with the promotion of diabetic wound repair [18].

As a star molecule, nitric oxide (NO) is one of the common endogenous gases signaling molecules [19], play an important role in regulating immunity, promoting wound healing [20], even the treatment of multiple diseases and many other physio-pathological conditions [21,22]. Their vasodilatory and boosting blood circulation properties may help transport nutrients to the damaged area for repair [23]. They promote angiogenesis [24], skin reconstruction, and wound recovery by increasing fibroblast migration [25] and collagen deposition [26]. They are also able to kill bacteria effectively through multiple mechanisms [27], such as lipid peroxidation [14], protein dysfunction [28], and DNA cleavage [29]. Additionally, NO is even capable of down-regulating inflammation [20,30]. These unique advantages are highly relevant to the existing difficulties in the treatment of diabetic foot ulcer. Consequently, NO promises to be a multifunctional antimicrobial agent in the treatment of diabetic foot bacterial infections and an attractive candidate for diabetic wound healing therapy. However, common NO donors such as nitroglycerin and Sodium Nitroprusside (SNP) are lack of controllability [31]. Their release of NO is spontaneous and occurs often in normal physiological environments [32]. In addition, the short half-life of NO also limits its therapeutic efficacy. Therefore, targeted delivery and controlled release of NO remains challenging. Herein, this is the significance of designing and developing a delivery system capable of accurately and controlled release of NO [33]. The on-demand generation of NO can be triggered in different ways [20], including endogenous biochemical stimulation and exogenous physical stimulation [34,35]. Among them, phototherapy mediated by Near-infrared (NIR) has the advantages of long penetration depth, good compatibility [36], and avoidance of drug resistance [37]. Therefore, it is considered a candidate for controlled on-demand NO production.

Currently, advances in nanomedicine have led to significant progress in the development of nano drug delivery systems and many attempts have been made to integrate NO donors into various nanomaterials [20,38]. Among various synthetic polymers, peptide dendrimers stand out for their unique properties, which have positioned them as a new class of biomaterials [39–42]. They have many excellent features, such as well-defined architectures, highly-branched structures, good biocompatibility, multi-valency, modifiable surface functionality and so on [43–45]. These advantages endow peptide dendrimers the potential to serve as excellent delivery carriers. Studies have shown that L-arginine is an endogenous peptide NO donor [46] with good biocompatibility and ability to generate NO catalyzed by inducible NO synthase (iNOS) or in reaction with reactive oxygen species (ROS) [47,48]. Nowadays, few studies have been designed to select peptide dendrimers as NO donors. Therefore, we hypothesize that the construction of a peptide dendrimer with L-arginine as a terminal group, combining NO-production capacity and functional amplification feature, in the hope that it could be a superior NO donor with various advantages such as good biocompatibility, high ROS conversion, and gas production efficiency.

In this study, we took advantage of the low pH of the biofilm-infected microenvironment to design a butterfly-shaped amphiphilic peptide dendrimer as a controlled and on-demand nitric oxide donor. Based on the zeolitic imidazolate framework-8 (ZIF-8) [49] has outstanding advantages in the encapsulation and transportation of functional materials due to its large specific surface area, convenient synthesis, and stable physiological conditions, hence ZIF-8 was selected to co-deliver the photosensitizer Chlorin e6 (Ce6) and peptide dendrimer modified with L-arginine as terminal group. Thereby, we develop a nano-multidrug co-delivery system, denoted as Ce6&Butterfly-shaped Dendrimer@ZIF-8 (C&D@Z), shown in **Supporting Information**. This innovative system is anticipated to harness the synergistic effects of the butterfly-shaped amphiphilic peptide dendrimer and photodynamic therapy (PDT), enabling the precise and controlled release of NO upon NIR irradiation. As illustrated in Scheme 1, when the C&D@Z is applied to an infected wound, the encapsulated dendrimer and Ce6 would be released from ZIF-8 upon the stimulation of the biofilm microenvironment. Following NIR irradiation, a cascade of reactions is initiated where Ce6 generated high levels of ROS to kill bacteria, and the induced ROS reacts with the dendrimers to continuously generate NO, which not only enhances nanoparticle penetration into the biofilm to exert bactericidal activity but also aids in the wound repair and inflammation inhibition. Furthermore, the NO produced has the potential to react with ROS to form more potent reactive nitrogen species (RNS) to kill bacteria [50], enhancing the antimicrobial effect and accelerating the wound healing process through a cascade reaction. By combining anti-biofilm, anti-inflammatory, and angiogenic effects, we aim to facilitate effective healing of biofilm-infected wounds, address the challenges in the treatment, and provide a promising solution for DFU.

2. Experimental Section

2.1. Materials

Chlorine E6 (Ce6) was obtained from Frontier Scientific Chemicals (Logan, UT, USA). 1,3-Diphenylisobenzofuran (DPBF) was purchased from Sigma Aldrich (St. Louis, MO, USA). All amino acids were bought from the GL Biochem (Shanghai, China). Propargylamine, 4-(4,6-Dimethoxy-1,3,5-triazin-2-yl)-4-methylmorpholinium chloride (DMTMM), trifluoroacetic acid (TFA), and sodium ascorbate were from Aladdin Reagent Company (Shanghai, China). Zinc nitrate hexahydrate, was purchased from Sinopharm Chemical Reagent CO., Ltd (Shanghai, China). Griess Reagent kits, Triton X-100, and streptozotocin (STZ) were obtained from the Beyotime Biotechnology (Shanghai, China). Dulbecco's modified Eagle's medium (DMEM) and anhydrous dimethylacetamide (DMF) were bought from Adamas (Shanghai, China). Fetal bovine serum (FBS) was obtained from Sorfa (Beijing, China). 2-methylimidazole was acquired from J&K Chemical Reagent Co., Ltd. (Beijing, China). Tryptone, Yeast extract, and SYTO9 & propidium iodide (PI) Kit were all from Thermo Fisher Scientific Inc. (Waltham, Massachusetts, USA). Tryptic Soy Broth medium (TSB) was obtained from Hopebio Biotechnology Co., Ltd (Qingdao, China). Agar was bought from the Sangon biotech (Shanghai, China). Crystal violet staining solution was acquired from Beijing Solarbio Science & Technology Co., Ltd (Beijing, China). Blood Glucose meter and Test Strips were bought from Sinocare (Changsha, China). Oxford cups were purchased from Shanghai Titan Scientific Co., Ltd (Shanghai, China). The QuantiCyto mouse Tumor Necrosis Factor-α (TNF-α) ELISA kit was acquired from NeoBioscience Technology Co, Ltd (Shenzhen, China). *Staphylococcus aureus (S. aureus)* (ATCC 49775) and *Escherichia coli (E. coli)* (ATCC 25922) were obtained from the Fujian Key Laboratory of Drug Target Discovery and Structural and Functional Research. *Methicillin-resistant Staphylococcus aureus (MRSA)* (ATCC 700699) was acquired from Shanghai Luwei Technology Co., Ltd (Shanghai, China).

2.2. Characterization

We prepared C&D@Z, while Ce6@ZIF-8 (C@Z), Ce6&Arginine@ZIF-8 (C&A@Z), Ce6&X-Arginine@ZIF-8 (C&XA@Z), Ce6&Poly-Arginine@ZIF-8 (C&P@Z), and Ce6&X-Poly-Arginine@ZIF-8 (C&XP@Z) has been prepared as control nanoparticles (see **supporting information**). Transmission Electron Microscope (TEM) images were acquired using TEM (Tecnai G2, FEI, Oregon, USA). Drug loading efficiency (LE) and entrapment efficiency (EE) of material were measured by Ultraviolet–visible spectrophotometer (UV–vis) (UV-2600, Shimadzu, Kyoto, Japan) *via* the following equation:

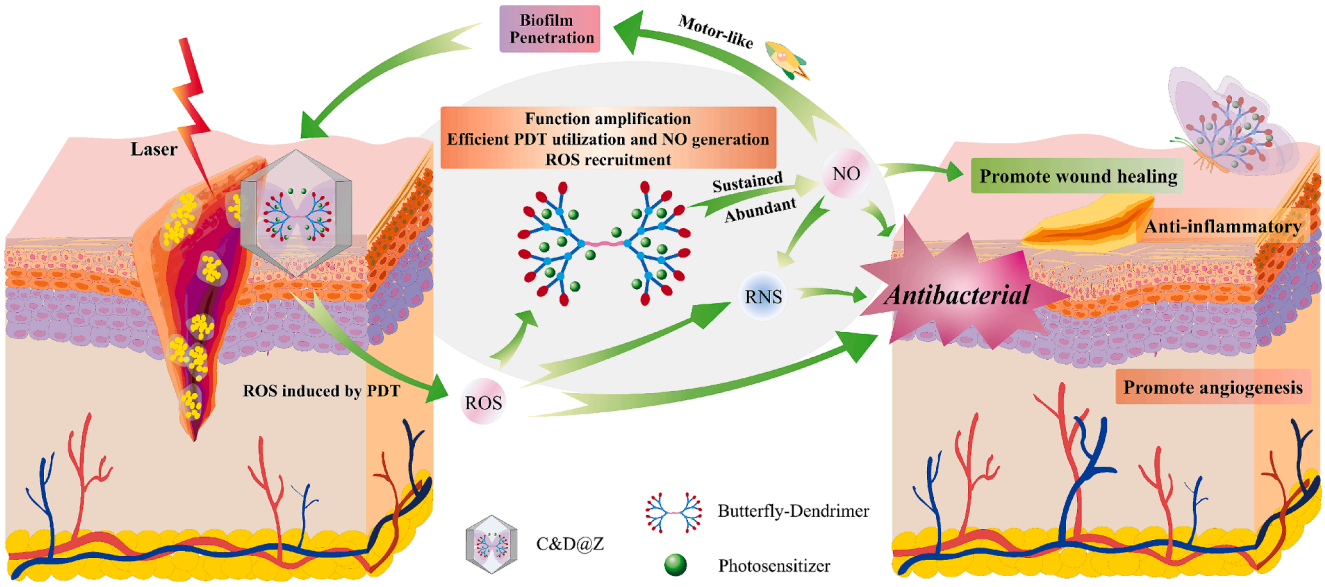

Scheme 1. Schematic diagram of C&D@Z based on butterfly-shaped amphiphilic peptide dendrimers for bactericidal, anti-inflammatory, and wound healing promotion in DFU infection treatment.

$$LE(\%) = \frac{m_1}{m_{C\&D@Z}} \times 100\% \quad (1)$$

$$EE(\%) = \frac{m_1}{m_2} \times 100\% \quad (2)$$

where m_1 and m_2 represent the measured mass and initial mass of Ce6 in C&D@Z.

The hydrodynamic diameter and zeta potential of the samples were measured on a Particle Analyzer (Litesizer 500, Anton Paar, Graz, Austria). The chemical structures of butterfly dendrimer and Poly-Arginine were characterized by Fourier Transform Infrared Spectroscopy (FT-IR) (iS50, Thermo, MA, USA).

2.3. Drug release assays

The drug release effect of C&D@Z was evaluated. To simulate the effect of different physiological environments on drug release, C&D@Z was incubated with 2 mL of phosphate buffer saline (PBS, pH 5.4 or 7.4) in a shaker at 37 °C. After centrifuged (8000 rpm, 10 min) at specific time points (0.33, 0.66, 1, 4, 8, and 12 h), 200 μL of supernatant was collected and resuspended by sonication. The drug concentration of Ce6 was determined by the characteristic UV absorption value at 660 nm. The cumulative release ratio was calculated by the following equation:

$$E = \left(\frac{V_E \sum_1^{n-1} C_i + V_0 C_n}{m_0} \right) \times 100\% \quad (3)$$

In this equation, E represents the cumulative release amount (%), V_E represents the sampling volume (200 μL), V_0 represents the initial volume (2 mL), C_i and C_n represent the measured drug concentrations (μg/mL), i and n represent the sampling times and m_0 represents the mass of Ce6 in C&D@Z (μg).

2.4. Profiles of ROS generation assessed via DPBF

The profiles of $^1O_2$ generation from C&D@Z + L were detected *via* 1,3-Diphenylisobenzofuran (DPBF, Sigma Aldrich, St. Louis, MO, USA). Firstly, different concentrations of C&D@Z, C&P@Z, and C&A@Z (equivalent Ce6: 0.15, 0.30, 0.60, 1.20, and 2.40 μg/mL) were mixed with an equal volume DPBF solution (10 μg/mL) solution in a 96-well plate, and then irradiated (660 nm, 5 mW/cm^2) for 3 min, respectively. In addition, C&D@Z, C&P@Z, and C&A@Z (concentration of Ce6: 0.60 μg/mL) mixed with an equal volume DPBF solution (10 μg/mL) solution in a 96-well plate were irradiated with different intensities (0.005, 0.050, 0.100, 0.250, 0.500, and 1.000 W/cm^2) for 3 min, respectively. Meanwhile, C@Z and free Ce6 (Ce6 concentration: 0.60 μg/mL) were also irradiated with the same volume of DPBF solution (10 μg/mL) in 96-well plates for different times (0, 2, 4, 6, 8, and 10 min). In all of these assays, PBS was set as a control group. The DPBF fluorescence was then measured using a Fluorescence Spectrophotometer (417 nm, Agilent Technologies, California, USA).

2.5. NO generation behaviour

The generation profiles of NO for C&D@Z with or without irradiation conditions were measured by Griess Reagent Kits. Briefly, C&D@Z, C&P@Z, and C&A@Z (equivalent Ce6: 125 μg/mL) were first mixed with equal volume Griess reagent I and II in a 96-well plate. The mixture was then irradiated (660 nm) at different intensities (0, 0.5, and 1.0 W/cm^2) for various durations (0, 1, 2, 3, 4, 5, 10, 15, and 20 min). At each time point, the amount of generated NO was determined by measuring the absorbance of the mixture using a microplate reader (540 nm, Multiskan GO, Thermo Fisher, MA, USA).

In addition, in order to evaluate the controllable release of NO gas during three on/off cycles, the NO generation profiles of C&D@Z were measured in parallel. In brief, C&D@Z, C&P@Z, C&A@Z, C&XP@Z, and C&XA@Z (equivalent Ce6: 125 μg/mL) were first mixed with equal volume Griess reagent I and II. Subsequently, the absorbance of the mixture, which underwent three on/off cycles irradiation (0.5 W/cm^2), was measured using a microplate reader (540 nm, Multiskan GO, Thermo Fisher, MA, USA) to determine the content of the generated NO.

2.6. The bacterial culture

S. aureus and *E. coli* were obtained from the Fujian Key Laboratory of Drug Target Discovery and Structural and Functional Research. *MRSA* was acquired from Shanghai Luwei Technology Co., Ltd (Shanghai, China). They were incubated in an incubator (SHP-250, Shanghai Jinghong technology Co., Ltd, Shanghai, China) at 37 °C.

The laser (660 nm, 0.5 W/cm^2, Changchun Laser Optoelectronics Technology Co., Ltd, Changchun, China) was selected for NIR irradiation in this work.

2.7. In vitro antibacterial activity evaluation

The *in vitro* antibacterial activity of C&D@Z was evaluated by the spread plate method. Briefly, the bacterial suspensions were washed with PBS, followed by resuspension and dilution to a concentration of 0.5×10^5 colony forming units (CFU)/mL using saline solution. Afterwards, the diluted bacterial suspensions were co-incubated with C&D@Z (equivalent Ce6 concentration of 0.3 μg/mL), C&P@Z, C&A@Z, or saline in a shaker at 37 °C for 0.5 h. Later, the mixture was irradiated for different time (0, 1, 2, and 3 min). At each time point, the treated bacterial suspensions were evenly spread on the agar plates and incubated for 48 h. Finally, the antibacterial effect of C&D@Z were monitored *via* counting the bacterial colonies. The same method has also been applied to *E. coli*. Not only that, the bacterial solution after different material treatments in this step was also inoculated into a new LB liquid medium, and the survival of the bacteria was observed by taking samples at different time points to determine the changes in absorbance value. In addition, C&D@Z treated agar plates were continuously incubated for 14 days, in order to observe whether there was still recurrent growth of the bacteria in the plates.

The antibacterial activity which influenced by the different concentration of C&D@Z was also measured in parallel. Briefly, diluted bacterial suspensions co-incubated with C&D@Z (Ce6 concentration: 0.1, 0.2, 0.3, 0.4, and 0.5 μg/mL) in a shaker at 37℃ for 0.5 h, while saline was set as control. After that, the mixture was irradiated for 2 min. At each time point, the treated bacterial suspensions were evenly spread on the agar plates and incubated for 48 h. The last, the bacterial colonies were counted to determine the antibacterial efficiency of C&D@Z.

2.8. Oxford cup assays

Oxford cup assays were further performed to analyze the antibacterial potential of C&D@Z against *S. aureus* by measuring the diameter of inhibition zone. First of all, a bacterial suspension (1×10^8 CFU/mL) were mixed with Luria-Bertani (LB) agar solution at 45 °C, the mixture was added into a sterile culture dish. After cooling and solidification, the Oxford cup was slowly placed in the center of the culture dish. And then, the sterile C&D@Z, C&P@Z, and C&A@Z (equivalent Ce6 concentration of 125 μg/mL) were added to the prepared Oxford cups, respectively. After 1 h of penetration and diffusion, they were irradiated for 5 min. Subsequently, the culture dishes were transferred to an incubator for another 48 h. Finally, the diameters of the inhibition zones were measured to study the antibacterial potential of the three materials.

2.9. Minimum inhibitory concentration assays

Minimum inhibitory concentration (MIC) of C&D@Z was visible to the naked eyes in a 96-well plate. The MIC is the lowest concentration of an antibacterial agent which would completely prevents visible growth of the bacteria. At first, the bacterial suspensions were washed with PBS, resuspended, and diluted to 10^7 CFU/mL using saline. Then, they were incubated with C&D@Z, C&P@Z, and C&A@Z (with equivalent Ce6 concentration of 0.25, 0.50, 1.00, 2.00, 4.00, and 8.00 μg/mL) in a 96-well plate. After irradiation for 2 min, they were further incubated for 48 h.

2.10. Biofilm culture

To prepare *S. aureus* biofilms, *S. aureus* suspension (1×10^8 CFU/mL) were firstly seeded into a confocal dish and incubated for 4 days. Subsequently, the culture medium was discarded and the biofilms adhered to the culture dish were harvested by gently washing away the planktonic bacteria with PBS thrice.

2.11. Evaluation of the ability to penetrate biofilms

Biofilms were prepared as described above. To begin with, C&D@Z (equivalent Ce6: 80 μg/mL), C@Z, and PBS were added on the biofilms in culture dishes and incubated for 12 h. Herein, the biofilms were irradiated for 5 min. Then, washed with PBS and labeled with SYTO-9 for 15 min. In the end, after washed with PBS, the treated biofilms were observed by Confocal Laser Scanning Microscope (CLSM) (SP5, Leica, Wetzlar, Germany).

2.12. Biofilm ablation validated by crystal violet (CV) staining, Scanning Electron Microscope (SEM), and Live&Dead staining

2.12.1. Crystal violet (CV) staining

CV staining assay was carried out to study the biofilm ablation effect of C&D@Z. Biofilms in 96-well plates were incubated with C&D@Z (Ce6 concentration: 5, 10, 50, and 100 μg/mL) in the dark for 4 h. Thereafter, the biofilms were irradiated for 8 min. Following incubation in the dark for another 1 h, they were washed with PBS and stained with 0.1 % CV for 0.5 h. Finally, the residual biofilms were rinsed with PBS and photographed by a digital camera.

2.12.2. SEM

Biofilm ablation effect was further assessed by SEM observation of bacterial morphology. The prepared biofilms attached on cover glasses were firstly incubated with C&D@Z (with equivalent Ce6: 137 μg/mL), free Ce6, and PBS in the dark for 12 h and then irradiated for 8 min. Wash with PBS, and fix in 2.5 % glutaraldehyde, followed by gradient dehydration and drying using an ion sputtering coater (Q150 R ES, Quorum, Laughton, UK). Eventually, the treated biofilms were observed by SEM (QUANTA 450, FEI, Oregon, USA).

2.12.3. Live&Dead staining

The biofilm ablation effect of C&D@Z was further estimated through the Live&Dead Assay utilize CLSM. The prepared biofilms attached on culture dishes were co-incubated with C&D@Z (concentration of Ce6: 80 μg/mL), C@Z, or PBS in the dark for 12 h. Later, the biofilms were irradiated for 5 min. Then washed with PBS and labeled with SYTO-9 (16.7 μM) and PI (100 μM) for 15 min. At last, the treated biofilms were washed with PBS and observed by CLSM (SP5, Leica, Wetzlar, Germany).

2.13. Hemolysis

Hemolysis assays were performed as follow: Initially, 1 mL fresh mouse blood was collected and added to the anticoagulant tube, centrifuged at 1,000 rpm for 10 min. The red blood cells (RBCs) were then washed and re-suspended with PBS to prepare the RBCs suspension. The suspension was mixed with C&D@Z (equivalent Ce6: 3.12, 6.25, 12.50, 25.00, 50.00, and 100.00 μg/mL), C&P@Z, C&A@Z, 1 % Triton X-100, or PBS. After that they were co-incubated for 1 h. The mixture was centrifuged at 12,000 rpm for 15 min, and the absorbance of the supernatant was gauged through a microplate reader (Multiskan GO, Thermo Fisher, 545 nm). The hemolysis ratio was determined *via* the following equation:

$$\text{Hemolysis rate}(\%) = \frac{A_{sample} - A_{negative}}{A_{positive} - A_{negative}} \times 100\% \quad (4)$$

2.14. In vivo anti-biofilm experiment

In order to assess the therapeutic efficacy of C&D@Z, ICR female mouse were purchased from Shanghai Slac Laboratory Animal Co., Ltd. And induced to develop diabetes by Streptozocin (STZ). Mouse with fasting blood glucose levels above 11 mmol/L in a week were regarded as diabetic [51]. They also showed diabetic symptoms of excessive

drinking and urination. A round full-thickness wound with diameter of 1 cm was created on their back, next inoculated with the *MRSA* suspension (1×10^8 CFU/mL) for 24 h to established wound infection. After that, the wounds were treated with C&D@Z at a Ce6 concentration of 100.00 μg/mL, C&P@Z, C&A@Z, C@Z, or PBS. Each treatment was followed by irradiation for 5 min, and the second administration was conducted two days later. The photographic record of the wound area and weight measurement were taken every two days throughout the 10 days treatment cycle. The bacterial residues at the wound site were collected for monitoring and evaluating wound healing of the infected mouse after the treatment was completed. At the end of the treatment, all mice were sacrificed, and wound skin tissue was collected for Hematoxylin and Eosin (H&E) staining, Masson staining, Vascular endothelial growth factor (VEGF) immunohistochemistry and CD86 immunofluorescence correlation analysis.

3. Results and Discussion

3.1. Preparation and characterization of C&D@Z

The butterfly-shaped peptide dendrimer and Poly-Arginine were successfully synthesized, and the detailed synthesis methods and characterization are shown in the **Supporting Information**. Then, we prepared C&D@Z, while C@Z, C&A@Z, C&XA@Z, C&P@Z and C&XP@Z were prepared as control nanoparticles. Through Dynamic light scattering (DLS) detection, C&D@Z was found to have mean hydrodynamic diameters of 83.97 nm and zeta potential of −17.0 mV (Fig. 1**A-B**). The Ce6 drug loading was 6.76 %, with encapsulation efficiency of 97.59 % as shown in Table 1. The results in Fig. 1**A-B**, and Table 1 also showed that the C@Z, C&A@Z, and C&P@Z displayed similar hydrodynamic diameters, zeta potential, drug loading, and encapsulation efficiency. The size of C&D@Z did not change significantly over a week (Fig. 1**F**),

Table 1
Drug loading efficiency (LE) and entrapment efficiency (EE) of different materials.

	EE (%)	LE (%)
C@Z	96.36	5.78
C&A@Z	99.57	4.98
C&P@Z	97.85	8.01
C&D@Z	97.59	6.76

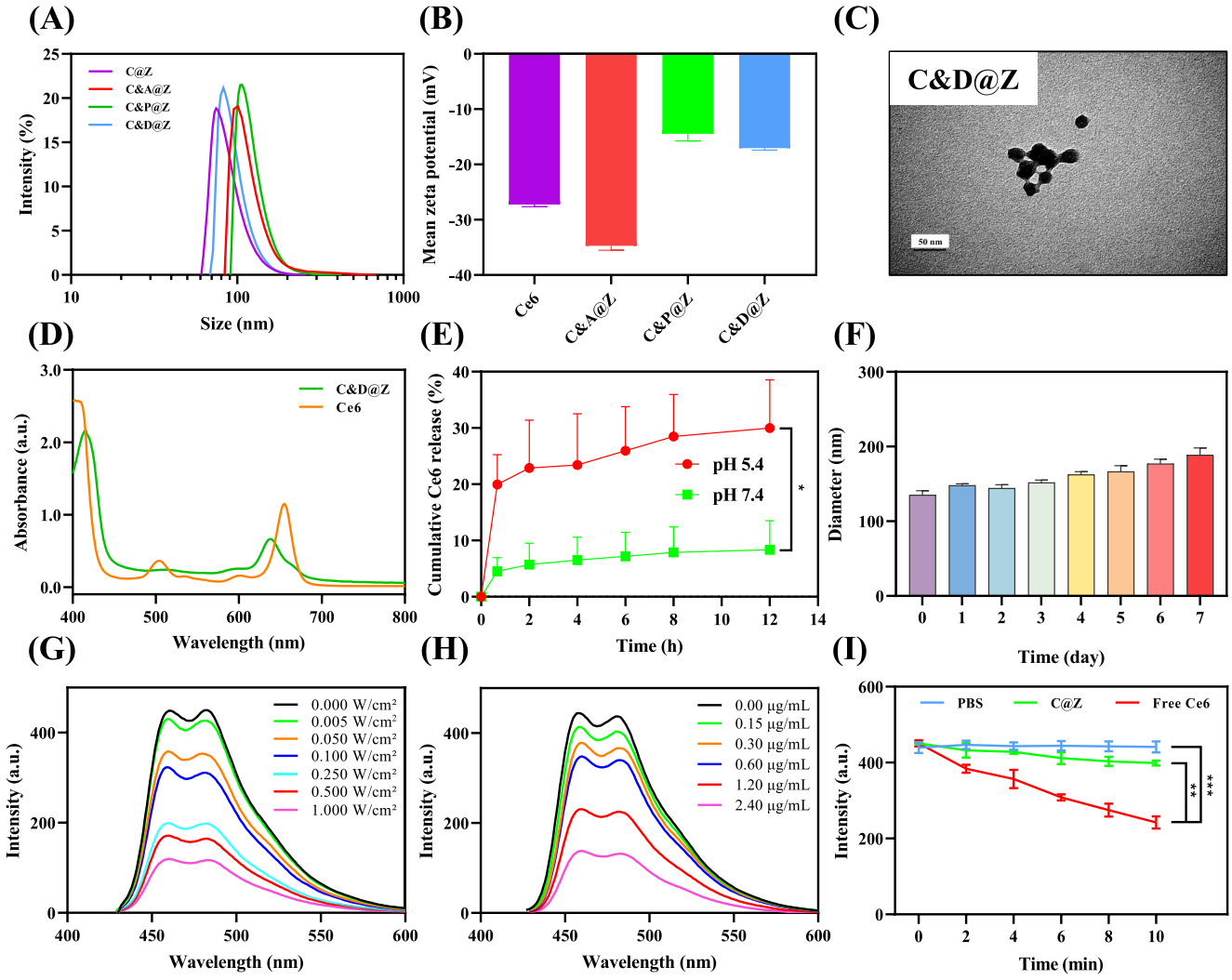

Fig. 1. A) Dynamic light scattering (DLS) of C@Z, C&A@Z, C&P@Z, and C&D@Z. B) Zeta potentials of Ce6, C&A@Z, C&P@Z, and C&D@Z (n = 3). C) TEM images of C&D@Z (scale bar: 50 nm). D) UV–vis absorption spectra of C&D@Z and Ce6 in PBS. E) The cumulated release curve of Ce6 from C&D@Z in PBS (pH 7.4 or 5.4) (n = 3). F) The size stability of C&D@Z in an aqueous solution for 7 days. ROS detection with DPBF (10 μg/mL) as a probe. G) DPBF co-incubated with C&D@Z (equivalent to 0.60 μg/mL Ce6 concentration) was irradiated with laser (660 nm, 3 min, the laser power range from 0-1.0 W/cm^2). H) DPBF co-incubated with different concentrations of C&D@Z (equivalent to Ce6) was irradiated with laser (660 nm, 3 min, 5 mW/cm^2). I) Fluorescence emission trend of DPBF treated with different materials (PBS, C@Z, and Free Ce6) (n = 3). Data are expressed as the mean ± SD, $^{**}p < 0.05$, $^{***}p < 0.001$.

showing excellent size stability. TEM images in Fig. 1**C** and **Fig. S4** exhibit that C&A@Z, C&P@Z, and C&D@Z displayed classic polyhedral morphology. Moreover, TEM analysis showed that the average hydrodynamic diameter of the nanoparticle is consistent with the DLS results. As shown in the UV–vis spectra of free Ce6 and C&D@Z (Fig. 1**D**), the main characteristic absorption peak of free Ce6 was located at 660 nm. In contrast, C&D@Z shows a decrease in peak height and a blueshift of the absorption peak around 640 nm, which proves the successful encapsulation of Ce6.

3.2. *In vitro drug release assays*

ZIF-8 is a class of nanomaterials with acid-responsive properties [49]. To evaluate the drug release profile, buffers with pH 5.4 and 7.4 were utilized to simulate the acidic microenvironment of the infection site and the neutral conditions of normal physiological environment, respectively. As observed in Fig. 1**E**, within the first 40 min, the release of Ce6 was significantly higher in the pH 5.4 buffer, reaching 19.94 %, compared to only 4.51 % in the pH 7.4 buffer. After 2h, the release of Ce6 in buffers of pH 5.4 and 7.4 could reach 22.87 % and 5.72 %, respectively, indicating a rapid initial drug release at pH 5.4. The release

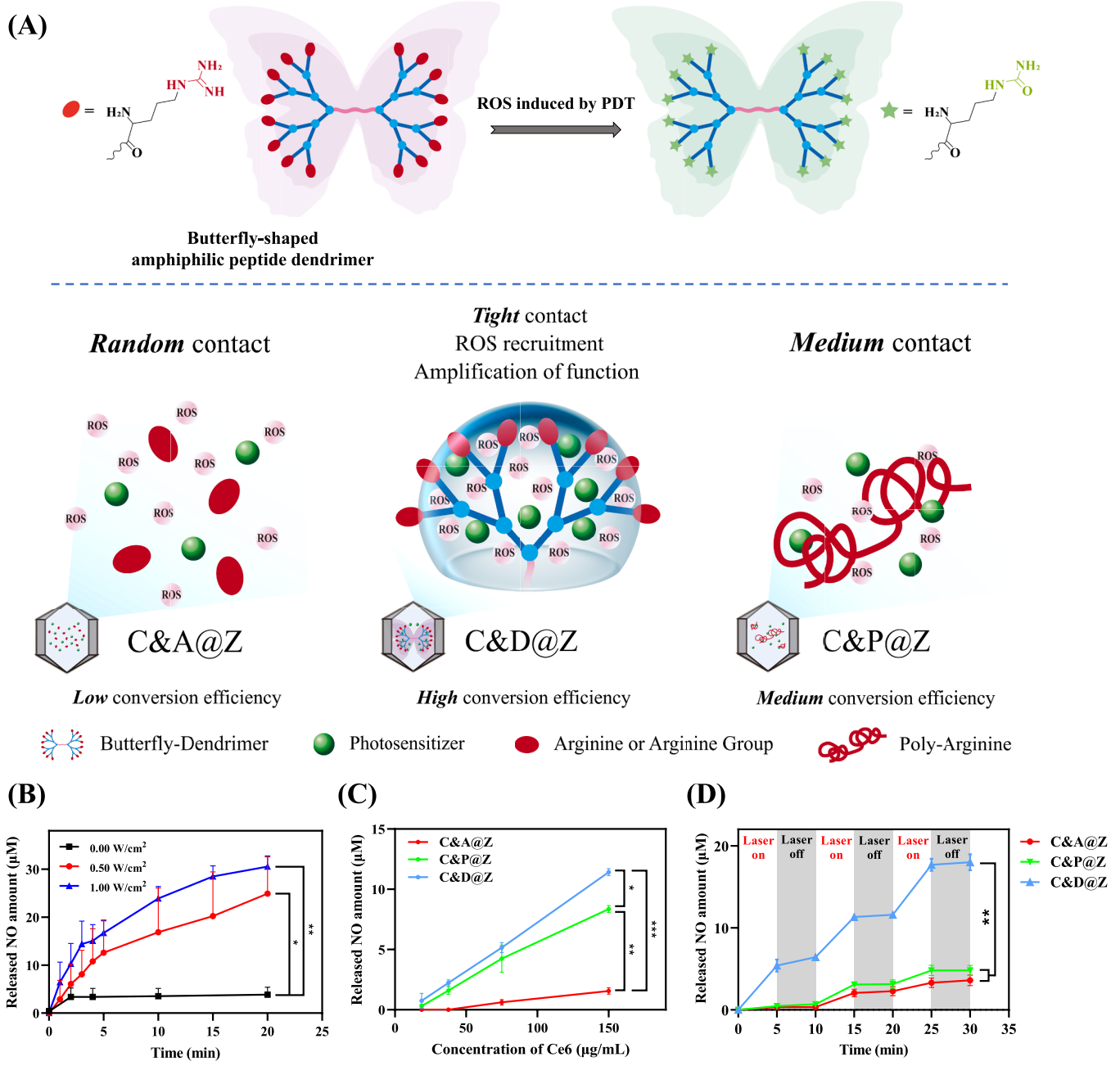

Fig. 2. A) Schematic illustration of the fundamentals of NO generation by butterfly-shaped amphiphilic peptide dendrimers and the NO generation of the C&A@Z, C&P@Z, and C&D@Z. Detection of NO with Griess reagent as the probe. B) Released NO amount of C&D@Z (equivalent to 125 μg/mL Ce6) after NIR irradiation with different power intensities (0.00, 0.50, and 1.00 W/cm^2). C) Quantification of NO released from C&A@Z, C&P@Z, and C&D@Z at different concentrations (equivalent to Ce6) after exposure to NIR irradiation (660 nm, 3 min, 0.5 W/cm^2). D) Controllable NO release profile of C&A@Z, C&P@Z, and C&D@Z (equivalent to Ce6 concentration: 125 μg/mL) under "ON/OFF" cycle laser irradiation conditions (660 nm, 0.5 W/cm^2). All the data are expressed as the mean ± SD (n = 3, *p < 0.05, **p < 0.01, ***p < 0.001).

then appeared to stabilize, with the pH 5.4 buffer showing a cumulative release of over 29.98 % after 12 h, whereas the pH 7.4 buffer released only 8.36 % of Ce6. Moreover, the release profile of Zn^{2+} showed similar results (**Fig. S5**). These findings demonstrate that C&D@Z is more sensitive to acidic microenvironment, which facilitates the selective release of the drug at the site of infection. Thus, C&D@Z has the potential to achieve sustained drug release in infected microenvironments.

3.3. Photodynamic properties studies of C&D@Z

1,3-diphenylisobenzofuran (DPBF) probe was employed to evaluate the $^1O_2$ generation. When DPBF was co-incubated with C&D@Z and illuminated by increasing intensity of 660 nm laser, the characteristic absorption peaks of DPBF gradually declined (Fig. 1**G**), indicating that the C&D@Z could generate ROS, causing a decrease in fluorescence. Meanwhile, as shown in Fig. 1**H**, NIR-irradiated C&D@Z could also trigger DPBF consumption in a concentration-dependent manner. Similarly, C&P@Z and C&A@Z also had similar properties to produce ROS (shown in **Fig. S6**). We also surprisingly found that when Ce6 was encapsulated into the ZIF-8 carrier, its ROS production ability was limited, showing less effective production than the free Ce6 (Fig. 1**I** and **Fig. S7**).

3.4. Efficient PDT recruitment enhances NO controllable generation from C&D@Z

Given that C&D@Z has been shown to possess the capability to produce reactive oxygen species (ROS), which is highly proportional to laser intensity and material concentration, we subsequently selected Griess Reagent Kits to evaluate the NO generation potential of C&D@Z induced by PDT. Fig. 2**A** is a brief schematic illustration of the C&D@Z to generate NO. As shown in Fig. 2**B**, few NO was detected in the group of C&D@Z without laser irradiation. Along with the increase of the laser power, a mass of colored products formed by the reaction of the generated NO with the kits was detected through a microplate reader. Under irradiation with a highest power of 1.00 W/cm^2, the released NO amount could up to about 30.56 μ M at 20 min. Correspondingly, C&P@Z and C&A@Z also had mild NO production capacity (shown in **Fig. S8**), but significantly weaker than C&D@Z, the NO released at the same laser irradiation power is only about 19.40 μM and 9.91 μM. What is more, as noted above, the quantity of generated NO gradually increases as the concentration of Ce6 in the material increases (Fig. 2**C**), and the trend was consistent with the previous results of the different laser power treated (Fig. 2**B** and **Fig. S8**). These results clearly illustrates that the C&D@Z has the best NO production capability, and the generating efficiency was depended on power and concentration. In addition, there is another remarkable point that the highly effective NO production behavior is directly related to the rational design of the dendrimer in the C&D@Z. Compared with poly-arginine and free L-arginine, butterfly dendrimer has a function amplification effect produced by its unique polyvalent (highly branched) structure, and the presence of abundant cavities in butterfly dendrimer help encapsulating the Ce6. Thus, the reason for the high efficiency of butterfly dendrimer in converting ROS to NO may arise from their internal voids and the extremely close distance between Ce6 and the arginine residues in dendrimer, enabling efficient recruitment of ROS in a short period of time as soon as generated by Ce6. Finally, together they contribute to the highest NO production [52].

Interestingly, PDT-Driven controllable NO generation was inspected during three on/off cycles (in Fig. 2**D**). When the laser was turned on, the C&D@Z rapidly released NO within 5 min. Conversely, NO was slowly produced when the laser was switched off. To further emphasize the excellent design of the C&D@Z, we additionally prepared the C&XP@Z and C&XA@Z with excessive amount of Poly-Arginine and Arginine added as illustrated in **Fig. S9**. With the introduce of excessive amount of Poly-Arginine or free L-Arginine, the NO they produced is hypothesized to be higher than the C&D@Z. However, the fact is that their NO production efficiency (8.8 μM for C&XP@Z and 7.6 μM for C&XA@Z in 5 min) were both still weaker than C&D@Z (approximately 18 μM in 5 min). This unusual finding probably further demonstrates that the rational design of our butterfly dendrimer as a highly efficient and controlled NO donor.

More surprisingly, even though we find that Ce6 encapsulated in ZIF-8 NPs is less efficient at ROS generation than free Ce6 (in Fig. 1**I** and **Fig. S7**), C&D@Z still has the ability to generate the most amount of NO. Consequently, C&D@Z could efficiently convert the limited ROS to the largest amount of NO due to its polyvalent structure and the presence of a large number of cavities. This result not only demonstrates the superiority of the butterfly dendrimer due to its rational design, but also proves that the butterfly dendrimer is a promising NO donor.

These results not only reflected that the release behavior of NO can be controlled by selective intermittent irradiation, and a large amount of NO is produced only when laser was received, but also demonstrated excellent photodynamic conversion of NO generation of the C&D@Z and highlight the excellent design of the butterfly dendrimer from another perspective, which may help to solve the shortcoming of not controlled release of NO donor drugs in prospect.

3.5. In-Vitro antibacterial activity Evaluation of C&D@Z

The *in-vitro* antibacterial activity of C&D@Z was evaluated by the standard plate count method. *S. aureus* suspension were incubated with C&A@Z, C&P@Z, and C&D@Z and treated by NIR irradiation in different time. Based on the results of the standard plate count (Fig. 3**A and S10**), we found that plenty of bacteria colonies existed on the plates which were without NIR treatment, indicating their negligible antibacterial activity in the absence of laser activation. With the NIR irradiation, the C&D@Z was able to complete the killing of all colonies in 3 min, while C&A@Z and C&P@Z still showed obvious colony growth. These results showed a highly effective bactericidal performance of the synergistic effect of ROS and NO. Inspired by the excellent antibacterial properties of the C&D@Z, we further investigated whether the colonies regrowth occurs during the 2-week period, studied the relationship between bactericidal ability and concentration of C&D@Z, examined the effect of C&D@Z on bacterial growth in liquid LB medium, and explore whether C&D@Z is effective in killing different species of bacteria, including Gram-negative bacteria *E. coli*. As displayed in Fig. 3**B**, there are no recurrent or new growth colonies on the plates of C&D@Z. With the ROS generated by Ce6, the ROS then rapidly oxidizes the arginine residues in butterfly dendrimer, and a possible further reaction occurs between ROS and NO to form RNS. This cascade reaction ultimately leads to C&D@Z having a superior sterilizing properties and possess the possibility of inhibiting the regrowth circumstance. Moreover, 0.5 μg/mL of C&D@Z is sufficient to reduce the bacterial viability to 5 % as shown in Fig. 3**D-E**. In addition, we monitored the growth curves of bacteria after treatment with different materials (C&A@Z, C&P@Z, and C&D@Z) during 13 h (Fig. 3**G**). Only in the group of C&D@Z, OD_{600} value remained relatively flat, which indicated that the C&D@Z could effectively kill all the bacteria upon a few minutes of irradiation. In contrast, C&A@Z and C&P@Z only slightly delayed the growth curve, and the bacteria could still continue to grow rapidly. It is pleasing to note that we found a similar killing effect of C&D@Z on *E. coli*, with a significant decrease in the number of colonies on the agar plates with increasing irradiation time (**Fig. S11**). These results further confirm that our designed C&D@Z possess a desirable antibacterial characterization.

Besides, the notable synergistic bactericidal ability of the C&D@Z was further proved using a Minimum Inhibitory Concentration (MIC) assay and an Oxford cup assay. First, the MIC values allows a clear visual comparison of the antimicrobial activity of C&D@Z, C&P@Z, and C&A@Z. We can see that the concentration corresponding to completely sterile wells of each material is clearly presented in Fig. 3**C**. Conspicuously, the C&D@Z having the smallest MIC value (1 μg/mL) among the

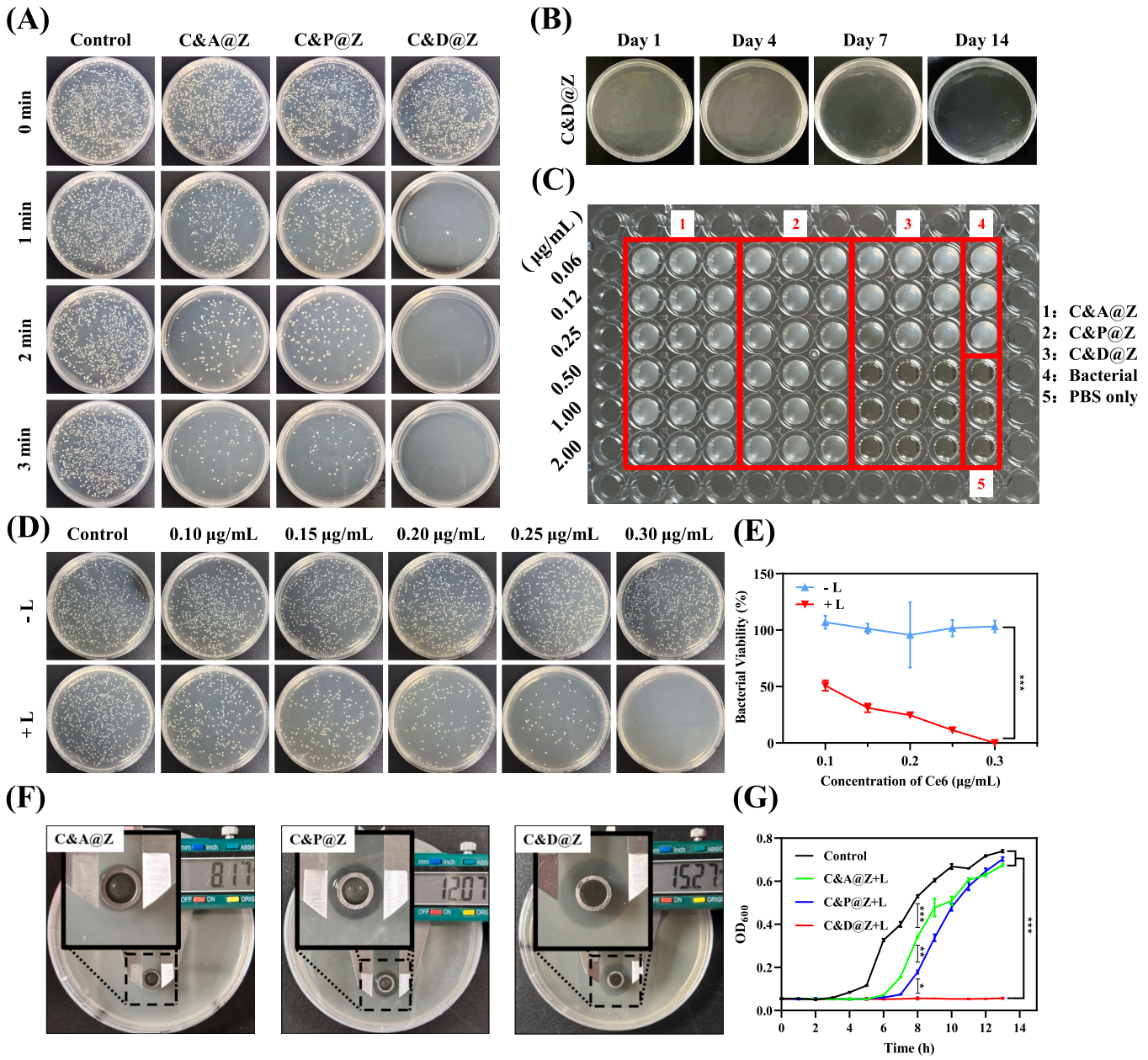

Fig. 3. A) Representative LB agar plates of *S. aureus* colonies after treatment with C&A@Z, C&P@Z, and C&D@Z (equivalent Ce6 concentration of 0.3 μg/mL) with varying durations of laser irradiation (n = 3). B) Regrowth inhibition of *S. aureus* by C&D@Z (equivalent to Ce6: 0.3 μg/mL) over a 14-day period. C) MIC of C&A@Z, C&P@Z, and C&D@Z (equivalent to Ce6) in 96-well plate (n = 3). D) Representative LB agar plates of *S. aureus* colonies after treated with different concentration (equivalent to Ce6) of C&D@Z with or without laser (660 nm, 2 min, 0.5 W/cm^2) and E) the semi-quantitative results (n = 3). F) Bacterial inhibition zones of C&A@Z, C&P@Z, and C&D@Z (equivalent Ce6 concentration of 125 μg/mL) irradiated with laser (660 nm, 5 min, 0.5 W/cm^2). G) Growth curves of *S. aureus* treated with different materials (C&A@Z + L, C&P@Z + L, and C&D@Z + L, equivalent to Ce6: 0.5 μg/mL) in 10 h. Data are expressed as the mean ± SD (n = 3). ***p < 0.001.

three materials (the MIC of the others at least 8 μg/mL) and demonstrating excellent in vitro antibacterial activity. Second, antimicrobial activity can also be demonstrated indirectly by measuring inhibition zone. The inhibition zone is formed by the limited effect of the materials on the growth of bacteria, and the inhibition zone is directly related to the constraint ability of the materials. As shown in Fig. 3**F, a** prominent inhibition zone formed in each of the materials, and the diameter of the C&D@Z inhibition zone (approximately 15.27 mm) was the biggest among the three materials. For C&A@Z and C&P@Z, the inhibition zones were much smaller, with diameters of only 8.17 mm and 12.07 mm, respectively. Combined with the results of the MIC and Oxford cup experiments, they together suggested that the C&D@Z has superior *in vitro* antibacterial activity.

3.6. *In vitro biofilm penetration performance of C&D@Z*

One of the preconditions for effective elimination of dense biofilms is the ability to penetrate deeply into the dense biofilm structure. The penetration of C&D@Z was investigated through the CLSM. The biofilms were stained with SYTO-9, and the penetration capability of C&D@Z was tracked by the fluorescence of Ce6. As shown in Fig. 4**A**, there was only few red fluorescence present in C@Z with or without Laser groups, demonstrating that the C@Z nanoparticles had limited penetration into the biofilm and resulted in a reduced therapeutic effect. Even after

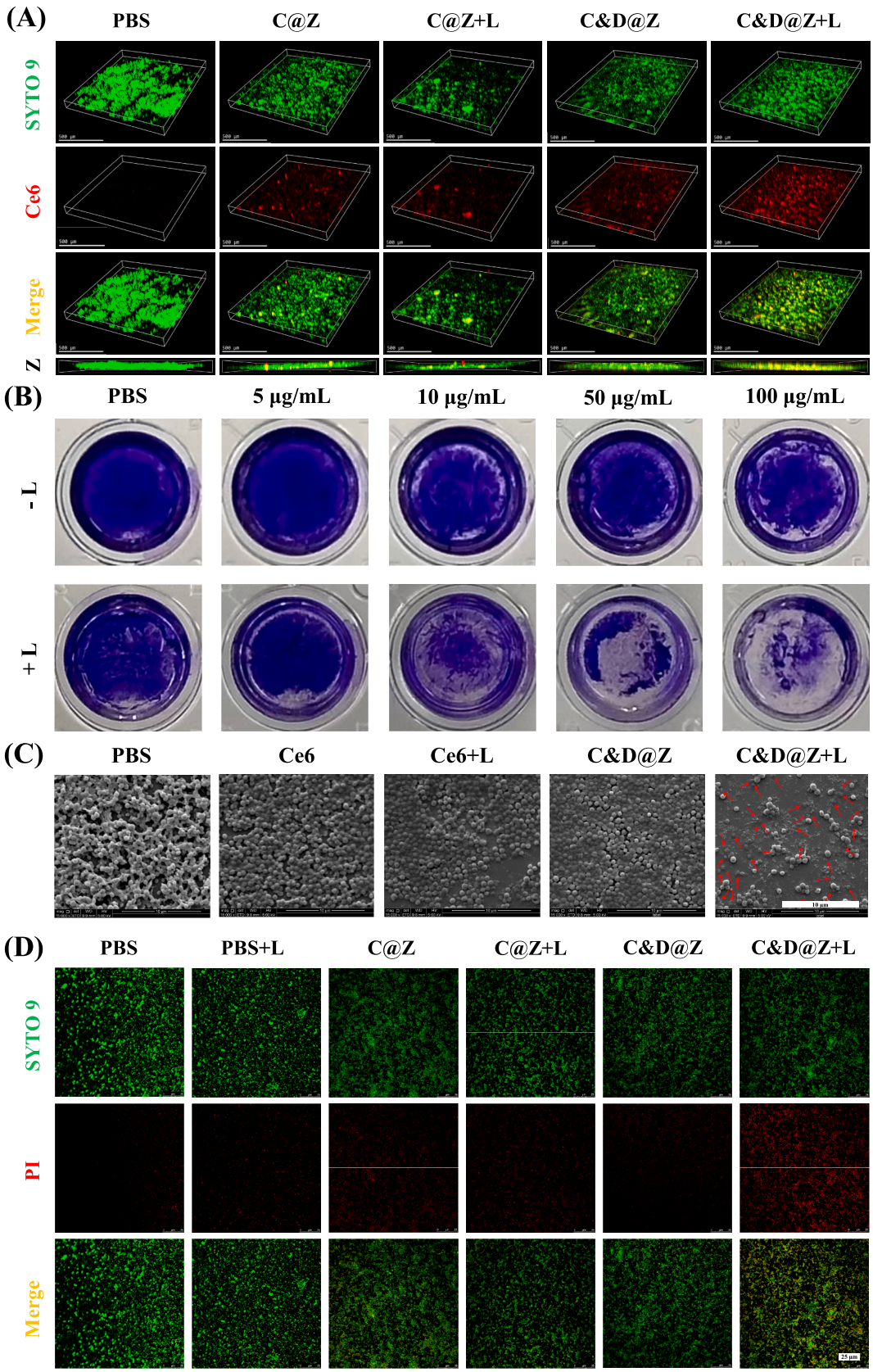

Fig. 4. A) CLSM images of biofilms under various treatments as indicated (Green fluorescence: biofilms stained with SYTO-9, Red fluorescence: Ce6 in C@Z or C&D@Z, scale bar: 500 μm). The images of the Z-axis are present in the fourth row. B) Biofilm biomass after treated with different concentration of C&D@Z with or without laser (stained with crystal violet). C) SEM images of *S. aureus* treated by Ce6 and C&D@Z with or without laser (red arrows: shrinkage, rupture, and surface collapse of *S. aureus*, scale bar: 10 μm). D) CLSM images of live (labeled with SYTO-9) and dead (stained with PT) bacteria in biofilms after different treatments, scale bar: 25 μm. In this study, +L indicates with laser, while −L means without laser.

incubating the biofilm with C&D@Z, the red fluorescence in the biofilm was still weak. Conversely, a strong red fluorescence signal was detected in the interior of the biofilm which treated with C&D@Z with laser irradiation. These results suggest that the large amount of NO produced by the laser trigger do endow C&D@Z a certain degree of biofilm permeability, which is expected to propel the C&D@Z from the surface to the deeper layers through the boost of the generated NO gas. The NO may act to disrupt the biofilm matrix and propel the delivery system deeper into the biofilm like a "motor", thereby enhancing the overall efficacy. In summary, the combination of NO generation and ROS production in C&D@Z + L appears to work synergistically, enabling deeper penetration through the biofilm matrix, which we hypothesize to be a result of the propulsive effects of NO, facilitating biofilm disruption and deeper penetration in a "motor-like" manner. Hence, it is the existence of the rational and superior design of C&D@Z that ultimately leads to the different penetration properties of C&D@Z and C@Z.

3.7. In vitro synergistic effect of PDT and NO on biofilm ablation

Inspired by the prominent penetration capability into biofilm and remarkable synergistic anti-bacterial efficiency of C&D@Z, with combination of PDT and NO, C&D@Z was expected to be effective in ablation of biofilms. To verify this, the biofilm biomass in the groups were treated with different concentrations of C&D@Z without laser irradiation and assayed *via* crystal violet staining. We found the biofilm was not particularly influenced by C&D@Z without laser irradiation (Fig. 4**B**), indicating that there is barely antibacterial activity for C&D@Z without laser trigger. Strikingly, we noticed that once laser irradiation is imposed, the biofilm biomass immediately reduced significantly with increasing concentrations of C&D@Z, this result clearly demonstrated the outstanding biofilm ablation efficacy of C&D@Z. Similarly, we compared the ablation effect of the C&A@Z, C&P@Z, and C&D@Z against biofilms (**Fig. S12**). None of the three materials showed obvious biofilm ablation in the absence of NIR irradiation. However, under NIR irradiation, C&D@Z was significantly ablated, reaching 88.81 %, whereas C&A@Z and C&P@Z only reached 69.5 % and 80.12 %, respectively. This result also provides strong evidence that differences in the ability to enter the deeper layers of the biofilm due to differences in NO production, ultimately affects the ablation of the biofilm.

Subsequently, the SEM observation was further performed to evaluate the ablation effect.The bacteria within the biofilms exposed to PBS retain intact and smooth spherical morphology, as illustrated in Fig. 4**C**. And biofilms look particularly thick overall. Meanwhile, we found that the thickness of biofilms in Ce6 and C&D@Z groups is thinner than those treated with PBS and exhibited obvious collapse, but all bacteria exhibited a fully intact cell membrane structures. The bacteria in biofilms treated with Ce6 and C&D@Z were also underwent metamorphosis, especially in the group of C&D@Z, where most of the bacteria became flattened. Although the biofilm in the group of Ce6 with laser (Ce6 + L) was thinner than that without laser irradiation, the biofilm treated with Ce6 + L still exhibits a well-structured and high-integrity cell membrane, indicating that the Ce6 + L has only negligible impact on biofilm ablation. (In this work, +L indicates with laser, while −L means without laser.) Additionally, majority of bacteria in the biofilm treated with C&D@Z + L was removed and eradicated, and the residual bacteria revealed severely collapse and contraction, even with leakage of cellular contents (marked with red arrow in Fig. 4**C**). The above results collectively illustrate that C&D@Z has the highly efficient synergistic bacterial ablation activity through the combination of PDT and NO.

To further explore the antibiofilm effect of C&D@Z, a bacterial live/dead staining assay was conducted using the SYTO 9/PI kit. SYTO 9 is a green fluorescent dye used for staining living and dead bacteria, and PI is a red fluorescent dye used for staining dead bacteria only with damaged membranes, respectively. Fig. 4**D** presents the fluorescent microscopy images of the biofilms following different treatments. And all of biofilms exhibited a bright green fluorescence, indicating the abundant presence of live and dead bacteria. Few red fluorescent spots were observed in either the PBS+/-L or C@Z+/-L groups, implying that the influence of irradiation or a single model of PDT had inadequate bactericidal effect for bacteria in biofilms. Compared with C&D@Z group, remarkably increased red fluorescence was found for the C&D@Z under light irradiation, indicating that the integration of PDT and NO can indeed destroy bacteria in the biofilm. Based on these results, we concluded that C&D@Z has great potential in ablating and eliminating bacterial biofilms. The abundant ROS generated by PDT could initially kill bacteria. Subsequently, the NO produced by oxidizing butterfly dendrimer promotes wound healing while killing bacteria. Ultimately, the more toxic RNS might generated by the further reaction of ROS with NO would continue to play a bactericidal role [50]. Besides, the generated NO induced by the PDT also could enhance the penetration of C&D@Z into the deeper biofilms.

3.8. In vivo antimicrobial and wound healing performance

To further assess blood compatibility, hemolysis assays were further carried out. All the hemolysis rates in different concentration of C&D@Z were less than 5 %, suggesting their well blood compatibility and potential for *in-vivo* application, as shown in **Fig. S13**.

Encouraged by the excellent *in vitro* antimicrobial and anti-biofilm capabilities of C&D@Z, we attempted to continue exploring whether C&D@Z has the potential to be further utilized for *in vivo* DFU combined with bacterial infection. Thus, a diabetic mouse *MRSA*-infected wound model was constructed to assess the *in vivo* antimicrobial/biofilm activity of C&D@Z and its potential for recovery promotion. Fig. 5**B and 5D** present representative photographs of the wound healing process in different treatment groups. It was obvious that after two administrations (scheme in Fig. 5**A**), especially the first one, the C&D@Z + L group had already demonstrated a significant decrease in wound area compared with the other groups and the trend is increasing over time. On day 10, the relative wound area in the C&D@Z + L group had significantly decreased to 7.88 %. In contrast, the relative wound areas in the other groups were as follows: Control at 50.05 %, Control + L at 31.47 %, C@Z + L at 38.73 %, C&A@Z + L at 51.92 %, C&P@Z + L at 32.54 %, and C&D@Z at 28.40 % (Fig. 5**C**). Notably, during the treatment period, mice in control groups exhibited subcutaneous varying degrees of pustules, whereas no pustules were found subcutaneously in any of the mice in the C&D@Z + L group. The representative pictures of the recovery process for each group shown in Fig. 5**B**, and the results of spread plates for the CFU of viable bacteria remaining within the infected wounds for each treatment group in Fig. 5**F**, it can be concluded that C&D@Z has superior antimicrobial properties when trigger by laser irradiation than others. It is also reasonable to hypothesize that the other groups suffer from insufficient bactericidal capacity to kill the bacteria at the site of infection, leading to the emergence of abscesses, as well as inflammation due to persistent infection hindering the healing process. Moreover, we also observed that none of the mice showed significant weight decrease after different treatment (Fig. 5**E**), indicating the biosafety of C&D@Z *in vivo*.

Diabetic wounds often exhibit an over-active inflammatory response, which can impede the healing process [53]. Hence, the therapeutic gas NO, which has anti-inflammatory properties, has the potential to promote wound healing [20]. Fig. 2**B** has shown that our designed C&D@Z has excellent NO production performance. To further investigate the anti-inflammatory effect of C&D@Z, the expression of the inflammatory factor TNF-α in the cell supernatants was evaluated. **Fig. S14** shows that both C&A@Z, C&P@Z, and C&D@Z, the expression levels of TNF-α in cell supernatant was decreased after NIR irradiation, and the C&D@Z + L group had the lowest expression level. The overall trend is also consistent with the observed differences in NO production among the three materials. These results indicate that C&D@Z can relieve inflammatory response by down-regulation of pro-inflammatory factors,

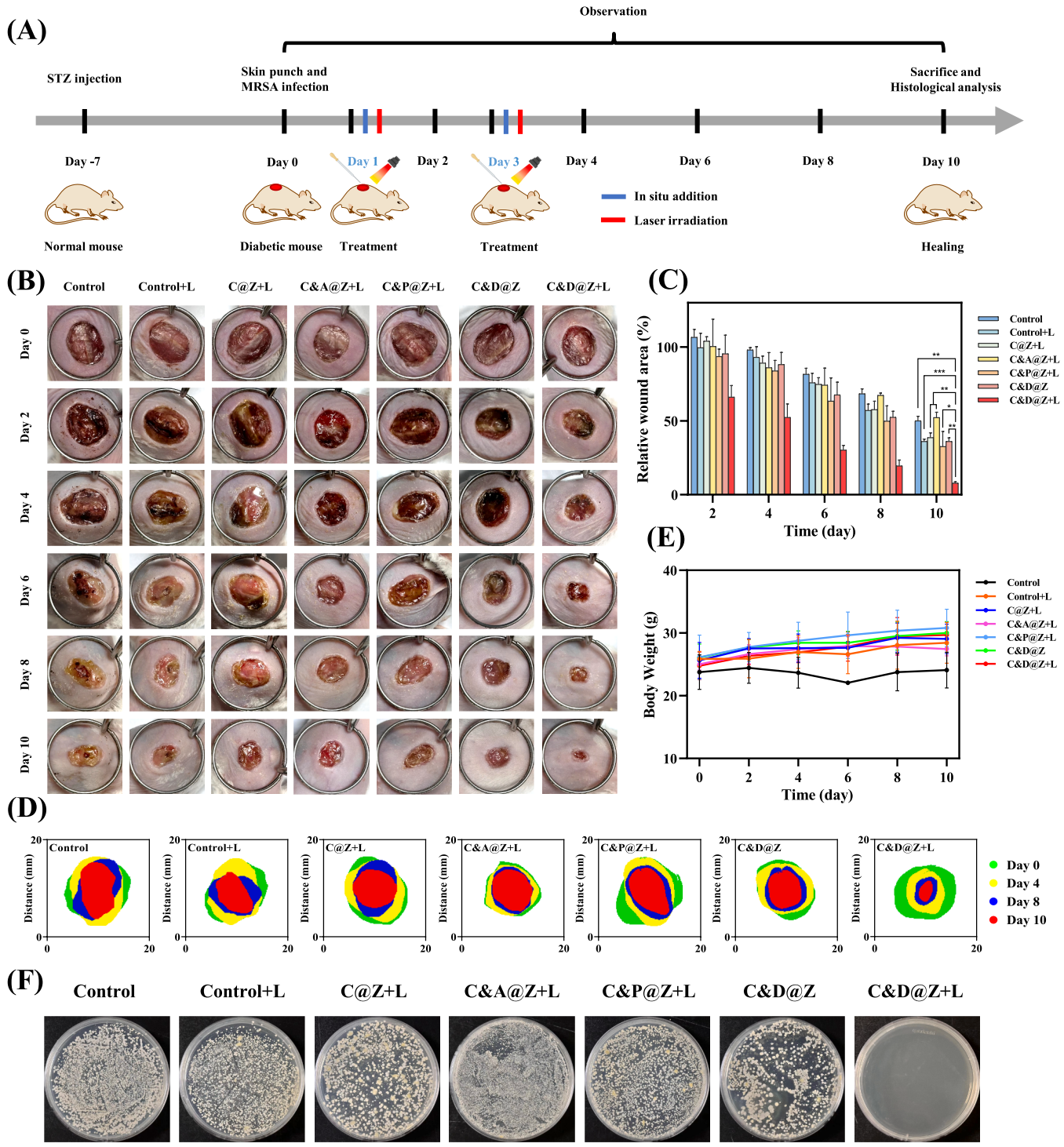

Fig. 5. A) Schematic representation for the establishment of the *MRSA* infection wound model in diabetic mice, the procedures of treatment, and assessment of wound healing. B) Photographs of the infected exposed wounds in mice following the administration of various treatments as indicated during 10 days, C) the semi-quantitative measurement of relative wound area (on day 2, 4, 6, 8, and 10, n = 3), and D) schematic diagram of the remaining wound area for each treatment group as indicated. E) The change of weight during treatment (n = 3). F) Results of LB agar plates. *MRSA* colonies that remained in the wound at the end of treatment for all groups were further detected *via* LB agar plates. All the data are expressed as the mean ± SD (n = 3, *$p < 0.05$, **$p < 0.01$, ***$p < 0.001$).

demonstrating the C&D@Z possess anti-inflammatory potential to alleviate excessive inflammation.

3.9. H&E staining and immunohistochemical assays

Wound healing is accompanied by a series of complex physiological processes, including inflammation, angiogenesis, and collagen deposition. At the end of the treatment, the recovery of the wound tissue was further evaluated using H&E and Masson staining. As shown in Fig. 6**A**, numerous aggregations and infiltrations of inflammatory cells (purple areas) were observed in the groups of Control, Control + L, C@Z + L, and C&D@Z, which was likely due to uncontrolled severe infection caused by *MRSA*. Compared with the control groups that showed infiltration of large amounts of inflammatory cells, the C&A@Z + L group

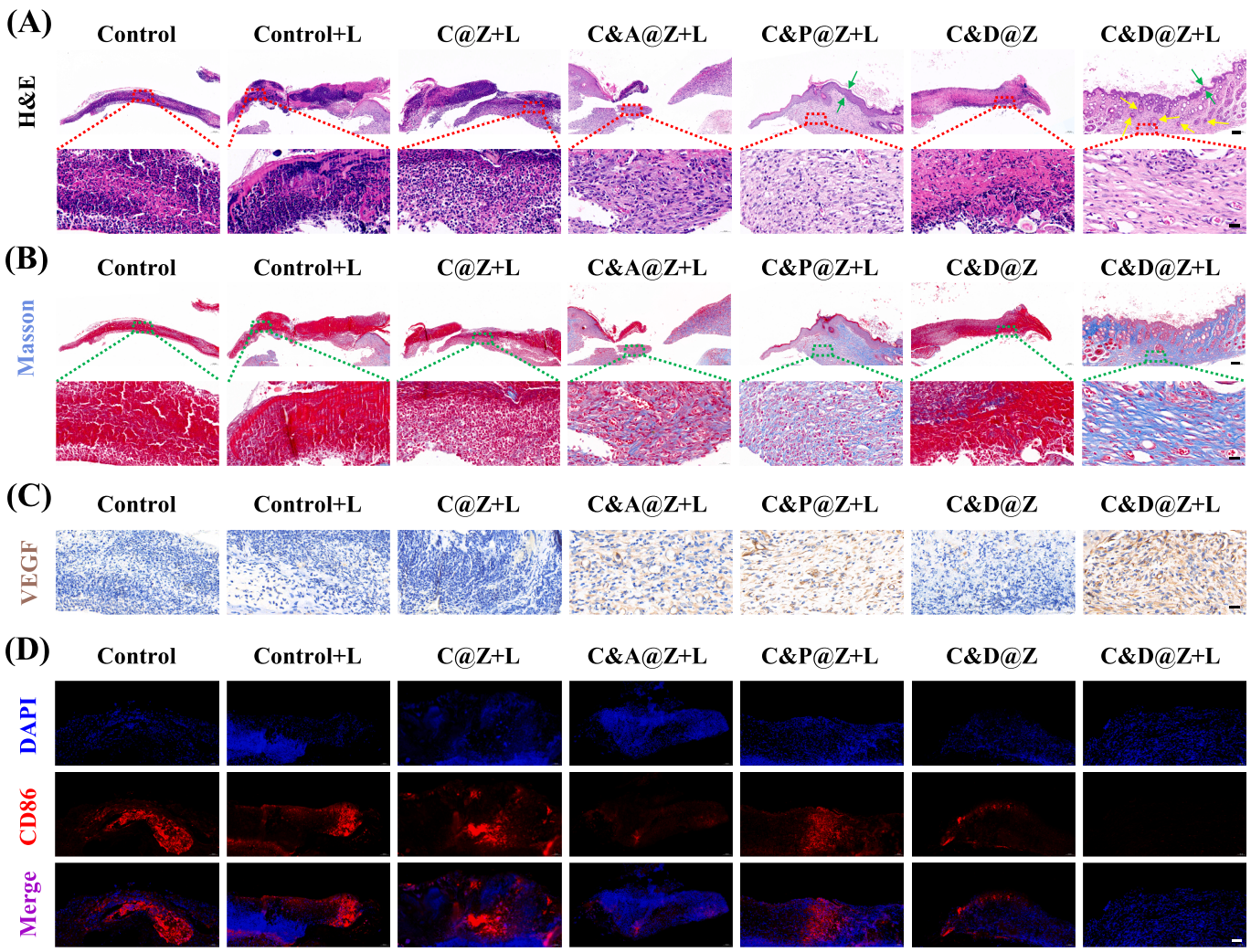

Fig. 6. The H&E, Masson, VEGF immunohistochemical staining, and immunofluorescence images of CD86 of infected wound tissues in the treated mice. A-D) Representative photomicrographs of wound tissues harvested at the end of study. And the groups were present as following: control, control + L, C@Z + L, C&A@Z + L, C&P@Z + L, C&D@Z, and C&D@Z + L. A) The purple areas indicate inflammatory cell infiltration (green arrows: epidermal layer, yellow arrows: hair follicles, scale bar: 100 μm (upper) and 20 μm (bottom). B) The blue areas indicate collagen deposition circumstance (scale bar: 100 μm (upper) and 20 μm (bottom)). C) The brown areas indicate VEGF-positive staining (scale bar is 20 μm). D) Immunofluorescence images of CD86 (red fluorescence) and nucleus (DAPI, signed as blue) in infected wounds after treatment (scale bar: 50 μm).

presented slightly reduced inflammatory infiltration in the wound tissues. Meanwhile, there were relatively less inflammatory cells aggregation and infiltration in the tissue after C&P@Z + L treatment, indicating the inflammation relief induced by NO therapy. It is exciting that the number of inflammatory cells was minimal in the C&D@Z + L group, and the histological structure was intact, with a thinner epidermal layer and a rich presence of healthy hair follicles visible (indicated by green and red arrows, respectively). These findings suggest that the synergistic effects of NO therapy and PDT, particularly the enhanced nitric oxide production capability of our designed C&D@Z, contribute to the excellent anti-inflammatory effects.

Collagen deposition plays a crucial role in the wound healing process, serving as a critical biomarker for assessing the progression and efficacy of tissue repair. As shown in Fig. 6**B**, the Masson staining confirmed that the C&D@Z + L group had significantly higher collagen deposition (blue areas) compared to the other groups, with coarse and well-aligned collagen fibers, indicating the superior formation of intact subcutaneous tissues and better recovery of the infected tissues. In contrast, few collagen fibers were observed in the other groups. Together, the H&E and Masson staining results suggest that C&D@Z not only reduces inflammation, but also accelerates wound healing by promoting collagen deposition, through NO gas therapy and its excellent bactericidal ability.

VEGF is essential in skin wound healing process. NO has been demonstrated to stimulate VEGF production, exert pro-angiogenic effects, and facilitate endothelial cell migration and proliferation [54]. As shown in the immunohistochemistry experiments (Fig. 6**C**), elevated levels of VEGF expression (brown areas) were found in the groups treated with C&A@Z + L, C&P@Z + L, and C&D@Z + L. Furthermore, the upregulated levels exhibited a positive correlation with the previously demonstrated NO production ability (Fig. 2**C**). The C&D@Z + L group showed the highest expression of VEGF levels, which was attributed to the beneficial effects of the most released NO. In contrast, few VEGF expressions were found in the other groups. These results suggest that the C&D@Z + L group has the highest level of angiogenesis and wound healing effects driven by NO generation.

The infection-induced pro-inflammatory microenvironment can cause an imbalance of immune homeostasis, characterized primarily by the overactivation of M1 macrophages [55,56]. Immunofluorescence staining was used to analyze the levels of pro-inflammatory M1 macrophage surface marker CD86 (red fluorescence). The absence of red fluorescence in the C&D@Z + L group indicated fewer M1-type

macrophages, suggesting that C&D@Z with laser irradiation improves the immune microenvironment of diabetic wounds. Moreover, the abundant NO produced from the butterfly dendrimer could relieve the inflammation to accelerate wound healing. In contrast, obvious red fluorescence was observed in all of the comparison groups (Fig. 6**D**). Even the C&A@Z + L and C&P@Z + L groups, which also has NO-producing capacity, exhibit limited improvement due to insufficient NO production. Red fluorescence remains evident, indicating extensive infiltration of pro-inflammatory M1-type macrophages and suggesting that the tissue remains in an inflammatory stage due to the high glycemic environment and persistent *MRSA* infection. Collectively, these results demonstrate that C&D@Z has excellent antimicrobial ability and, promotes collagen deposition and angiogenesis by modulating the immune microenvironment, and ultimately contributes to effective healing of diabetic wounds.

4. Conclusion

In summary, our study presents a novel nanoscale multidrug delivery system, C&D@Z, which has been engineered to combat *MRSA* and enhance the healing of DFUs. This system leverages a synergistic cascade reaction initiated by PDT and NO therapy generated from peptide dendrimer, demonstrating controlled and on-demand generation of ROS and NO under NIR irradiation. The production of NO acts as a propelling motor, facilitating the system to penetrate deeper into the biofilm. Notably, C&D@Z exhibits the strongest NO production efficiency, exceptional biofilm permeability, and superior antibacterial activity, outperforming all other control materials in *in-vitro* experiments. *In vivo* studies using a diabetic mouse model with *MRSA*-infected full-thickness skin wounds have further revealed that the C&D@Z had an outstanding effect in promoting wound healing. The delivery system not only eradicates *MRSA* but also stimulates angiogenesis and enhances collagen deposition through a cascade reaction mechanism. Additionally, C&D@Z harnesses the anti-inflammatory properties of NO, effectively reducing inflammation by modulating the expression of inflammatory mediators and decreasing the number of M1-type macrophages. This comprehensive approach integrates the advantages of peptide dendrimers, PDT, and NO therapy to address the complex challenges posed by bacterial infections in diabetic foot ulcers. Our findings demonstrate the potential of C&D@Z as a promising therapeutic strategy for the treatment of diabetic-infected wounds, offering a significant candidate and strategy in the field of wound care and antimicrobial therapy.

CRediT authorship contribution statement

Xiangyu Huang: Writing – review & editing, Writing – original draft, Methodology, Investigation, Formal analysis, Data curation. **Zucheng Shen:** Writing – review & editing, Writing – original draft, Methodology. **Qi Deng:** Writing – review & editing, Methodology. **Chengfei Zhao:** Writing – review & editing, Methodology, Funding acquisition. **Xiaofeng Cai:** Writing – review & editing, Methodology, Data curation. **Shaoteng Huang:** Writing – review & editing, Methodology, Formal analysis. **Mingbo Zhang:** Writing – review & editing, Methodology. **Yanzhuo Lv:** Writing – review & editing, Methodology. **Dongliang Yang:** Writing – review & editing, Methodology, Conceptualization. **Junyang Zhuang:** Writing – review & editing, Methodology, Conceptualization. **Ning Li:** Writing – review & editing, Writing – original draft, Supervision, Project administration, Methodology, Funding acquisition, Conceptualization.

5. Funding

This work was supported by National Natural Science Foundation of China (51703245) and Natural Science Foundation of Fujian Province (2024J01499 and 2023J01160). The present study was supported in part by the grant from Guangxi Key Laboratory of Molecular Medicine in Liver Injury and Repair (GXLIRMMKL-K202403).

Declaration of competing interest

The authors declare the following financial interests/personal relationships which may be considered as potential competing interests: Ning Li reports financial support was provided by National Natural Science Foundation of China. Ning Li reports financial support was provided by Natural Science Foundation of Fujian Province. Chengfei Zhao reports financial support was provided by Natural Science Foundation of Fujian Province. Ning Li reports financial support was provided by Guilin Medical University Affiliated Hospital Guangxi Key Laboratory of Molecular Medicine in Liver Injury and Repair. If there are other authors, they declare that they have no known competing financial interests or personal relationships that could have appeared to influence the work reported in this paper.

Acknowledgements

[#]Xiangyu Huang, Zucheng Shen, and Qi Deng contributed equally to this work. The authors would like to thank Minxia Wu and Xi Lin from Public Technology Service Center of Fujian Medical University; Prof. Shaohuang Weng, Prof. Weiming Sun, and Quanhui Fang from the School of Pharmacy, Fujian Medical University; Doctor Tao Wang from the School and Hospital of Stomatology, Fujian Stomatological Hospital, Fujian Medical University for their technical assistance.

Ethical approval.

The animal study protocol and experiments have been approved by the Ethical Committee of Fujian Medical University (No. IACUC FJMU 2024-0309) and conducted by following the guidelines from the Ethics Committee and national regulations of China.

Appendix A. Supplementary data

Supplementary data to this article can be found online at https://doi.org/10.1016/j.cej.2025.159380.

Data availability

Data will be made available on request.

References

[1] M. Wang, Z. Zhang, Q. Huo, M. Wang, Y. Sun, H. Liu, J. Chang, B. He, Y. Liang, Targeted polymeric nanoparticles based on mangiferin for enhanced protection of pancreatic β-cells and type 1 diabetes mellitus efficacy, ACS Appl. Mater. Interfaces 14 (9) (2022) 11092–11103.
[2] H.-Y. Su, C.-Y. Yang, H.-T. Ou, S.-G. Chen, J.-C. Chen, H.-J. Ho, S. Kuo, Cost-effectiveness of novel macrophage-regulating treatment for wound healing in patients with diabetic foot ulcers from the taiwan health care sector perspective, JAMA Netw. Open 6 (1) (2023) e2250639.
[3] F. Huang, X. Lu, Y. Yang, Y. Yang, Y. Li, L. Kuai, B. Li, H. Dong, J. Shi, Microenvironment-based diabetic foot ulcer nanomedicine, Adv. Sci. 10 (2) (2023) e2203308.
[4] M. Wang, Y. Liang, K. Chen, M. Wang, X. Long, H. Liu, Y. Sun, B. He, The management of diabetes mellitus by mangiferin: advances and prospects, Nanoscale 14 (6) (2022) 2119–2135.
[5] J. Chen, D. Chen, J. Chen, T. Shen, T. Jin, B. Zeng, L. Li, C. Yang, Z. Mu, H. Deng, X. Cai, An all-in-one CO gas therapy-based hydrogel dressing with sustained insulin release, anti-oxidative stress, antibacterial, and anti-inflammatory capabilities for infected diabetic wounds, Acta. Biomater. 146 (2022) 49–65.
[6] S. Chen, Y. Yu, S. Xie, D. Liang, W. Shi, S. Chen, G. Li, W. Tang, C. Liu, Q. He, Local H_2 release remodels senescence microenvironment for improved repair of injured bone, Nat. Commun. 14 (1) (2023) 7783.
[7] J.W. Costerton, P.S. Stewart, E.P. Greenberg, Bacterial biofilms: a common cause of persistent infections, Science 284 (5418) (1999) 1318–1322.
[8] C. Li, Y.X. Zhu, Y. Yang, W. Miao, X. Shi, K.F. Xu, Z.H. Li, H. Xiao, F.G. Wu, Bioinspired multifunctional cellulose film: *in situ* bacterial capturing and killing for managing infected wounds, Bioact. Mater. 36 (2024) 595–612.
[9] X. Lv, L. Wang, A. Mei, Y. Xu, X. Ruan, W. Wang, J. Shao, D. Yang, X. Dong, Recent nanotechnologies to overcome the bacterial biofilm matrix barriers, Small 19 (6) (2023) e2206220.

[10] Q. Xu, Q. Li, M. Ding, W. Xiu, B. Zhang, Y. Xue, Q. Wang, D. Yang, H. Dong, Z. Teng, Y. Mou, Flexible nanoplatform facilitates antibacterial phototherapy by simultaneously enhancing photosensitizer permeation and relieving hypoxia in bacterial biofilms, Acta. Biomater. 184 (2024) 313–322.

[11] Y. Wang, H.D. Shi, H.L. Zhang, Y. Yu Chen, B. Ren, Q. Tang, Q. Sun, Q.L. Zhang, J. G. Liu, A multifunctional nanozyme with NADH dehydrogenase-like activity and nitric oxide release under near-infrared light irradiation as an efficient therapeutic for antimicrobial resistance infection and wound healing, Adv. Healthc. Mater. 12 (25) (2023) 2300568.

[12] Y. Hu, X. Ruan, X. Lv, Y. Xu, W. Wang, Y. Cai, M. Ding, H. Dong, J. Shao, D. Yang, X. Dong, Biofilm microenvironment-responsive nanoparticles for the treatment of bacterial infection, Nano Today 46 (2022) 101602.

[13] Y.F. Li, L. Hua, W. He, L. Chen, Y.Z. Piao, M.N. Peng, D.D. Li, L.Q. Shi, Y. Liu, Microenvironment-adaptive metallo-polymeric nanodecoys *via* subcomponent coordination for bacterial biofilm eradication and immunomodulation, Adv. Funct. Mater. 2405487 (2024).

[14] W. Feng, M. Chitto, W. Xie, Q. Ren, F. Liu, X. Kang, D. Zhao, G. Li, T.F. Moriarty, X. Wang, Poly(d-amino acid) nanoparticles target staphylococcal growth and biofilm disassembly by interfering with peptidoglycan synthesis, ACS Nano 18 (11) (2024) 8017–8028.

[15] W. Xiu, L. Wan, K. Yang, X. Li, L. Yuwen, H. Dong, Y. Mou, D. Yang, L. Wang, Potentiating hypoxic microenvironment for antibiotic activation by photodynamic therapy to combat bacterial biofilm infections, Nat. Commun. 13 (1) (2022) 3875.

[16] Y. Su, Z. Zhi, Q. Gao, M. Xie, M. Yu, B. Lei, P. Li, P.X. Ma, Autoclaving-derived surface coating with *in vitro* and *in vivo* antimicrobial and antibiofilm efficacies, Adv. Healthc. Mater. 6 (6) (2017) 1601173.

[17] J.J. Li, Y. Hu, B. Hu, W. Wang, H. Xu, X.Y. Hu, F. Ding, H.B. Li, K.R. Wang, X. Zhang, D.S. Guo, Lactose azocalixarene drug delivery system for the treatment of multidrug-resistant pseudomonas aeruginosa infected diabetic ulcer, Nat. Commun. 13 (1) (2022) 6279.

[18] H. Li, J. Jiang, X. Lv, Y. Xu, W. Wang, D. Yang, X. Dong, Enzyme-like photocatalytic octahedral Rh/Ag_2MoO_4 accelerates diabetic wound healing by photo-eradication of pathogen and relieving wound hypoxia, Small (2024) e2402723.

[19] K. Zhang, H. Xu, X. Jia, Y. Chen, M. Ma, L. Sun, H. Chen, Ultrasound-triggered nitric oxide release platform based on energy transformation for targeted inhibition of pancreatic tumor, ACS Nano 10 (12) (2016) 10816–10828.

[20] S.M. Andrabi, N.S. Sharma, A. Karan, S.M.S. Shahriar, B. Cordon, B. Ma, J. Xie, Nitric oxide: physiological functions, delivery, and biomedical applications, Adv. Sci. 10 (30) (2023) 2303259.

[21] J. Sun, X. Cai, C. Wang, K. Du, W. Chen, F. Feng, S. Wang, Cascade reactions by nitric oxide and hydrogen radical for anti-hypoxia photodynamic therapy using an activatable photosensitizer, J. Am. Chem. Soc. 143 (2) (2021) 868–878.

[22] F. Wang, J. Wu, M. Yuan, Z. Yan, X. Liu, W. Li, Y. Zhang, C. Sheng, N. Liu, Z. Huang, Novel nitric oxide donor-azole conjugation strategy for efficient treatment of cryptococcus neoformans infections, J. Med. Chem. 66 (20) (2023) 14221–14240.

[23] C.-H. Su, W.-P. Li, L.-C. Tsao, L.-C. Wang, Y.-P. Hsu, W.-J. Wang, M.-C. Liao, C.-L. Lee, C.-S. Yeh, Enhancing microcirculation on multitriggering manner facilitates angiogenesis and collagen deposition on wound healing by photoreleased NO from hemin-derivatized colloids, ACS Nano 13 (4) (2019) 4290–4301.

[24] X. Zhang, Y. Zhang, R. Zhang, X. Jiang, A.C. Midgley, Q. Liu, H. Kang, J. Wu, A. Khalique, M. Qian, D. An, J. Huang, L. Ou, Q. Zhao, J. Zhuang, X. Yan, D. Kong, X. Huang, Biomimetic design of artificial hybrid nanocells for boosted vascular regeneration in ischemic tissues, Adv. Mater. 34 (14) (2022) e2110352.

[25] Y. Yang, K. Huang, M. Wang, Q. Wang, H. Chang, Y. Liang, Q. Wang, J. Zhao, T. Tang, S. Yang, Ubiquitination flow repressors: enhancing wound healing of infectious diabetic ulcers through stabilization of polyubiquitinated hypoxia-inducible factor-1α by theranostic nitric oxide nanogenerators, Adv. Mater. 33 (45) (2021) e2103593.

[26] S. Huang, S. Xu, Y. Hu, X. Zhao, L. Chang, Z. Chen, X. Mei, Preparation of NIR-responsive, ROS-generating and antibacterial black phosphorus quantum dots for promoting the MRSA-infected wound healing in diabetic rats, Acta Biomater. 137 (2022) 199–217.

[27] Y. Xu, J. Jiang, X. Lv, H. Li, D. Yang, W. Wang, Y. Hu, L. Liu, X. Dong, Y. Cai, Environment-triggered nanoagent with programmed gas release performance for accelerating diabetic infected wound healing, Chem. Eng. J. 479 (2024) 147645.

[28] Z.H. Chen, H.T. Zhang, Y. Lyu, K. Lv, H. Xing, P.F. Shen, Z.X. Guo, G.W. Li, D. Ma, Octopus-inspired adaptive molecular motion for synergistic photothermal and nitric oxide antibacterial therapy in diabetic wound repair, Adv. Funct. Mater. 2402591 (2024).

[29] Q. Gao, X. Zhang, W. Yin, D. Ma, C. Xie, L. Zheng, X. Dong, L. Mei, J. Yu, C. Wang, Z. Gu, Y. Zhao, Functionalized MoS_2 nanovehicle with near-infrared laser-mediated nitric oxide release and photothermal activities for advanced bacteria-infected wound therapy, Small 14 (45) (2018) e1802290.

[30] G. Yang, D.Y. Wang, Y. Liu, F. Huang, S. Tian, Y. Ren, J. Liu, Y. An, H.C. van der Mei, H.J. Busscher, L. Shi, In-biofilm generation of nitric oxide using a magnetically-targetable cascade-reaction container for eradication of infectious biofilms, Bioact. Mater. 14 (2022) 321–334.

[31] Z. Huang, J. Fu, Y. Zhang, Nitric oxide donor-based cancer therapy: advances and prospects, J. Med. Chem. 60 (18) (2017) 7617–7635.

[32] Z. Yuan, C. Lin, Y. He, B. Tao, M. Chen, J. Zhang, P. Liu, K. Cai, Near-infrared light-triggered nitric-oxide-enhanced photodynamic therapy and low-temperature photothermal therapy for biofilm elimination, ACS Nano 14 (3) (2020) 3546–3562.

[33] H. Xing, H. Peng, Y. Yang, K. Lv, S. Zhou, X. Pan, J. Wang, Y. Hu, G. Li, D. Ma, Nitric oxide synergizes minoxidil delivered by transdermal hyaluronic acid liposomes for multimodal androgenetic-alopecia therapy, Bioact. Mater. 32 (2024) 190–205.

[34] F. Li, J. Yan, C. Wei, Y. Zhao, X. Tang, L. Xu, B. He, Y. Sun, J. Chang, Y. Liang, "Cicada out of the shell" deep penetration and blockage of the HSP90 pathway by ROS-responsive supramolecular gels to augment trimodal synergistic therapy, Adv. Sci. 11 (25) (2024) e2401214.

[35] X. Jia, Y. Zhang, Y. Zou, Y. Wang, D. Niu, Q. He, Z. Huang, W. Zhu, H. Tian, J. Shi, Y. Li, Dual Intratumoral redox/enzyme-responsive NO-releasing nanomedicine for the specific, high-efficacy, and low-toxic cancer therapy, Adv. Mater. 30 (30) (2018) e1704490.

[36] J. Jiang, X. Lv, H. Cheng, D. Yang, W. Xu, Y. Hu, Y. Song, G. Zeng, Type I photodynamic antimicrobial therapy: principles, progress, and future perspectives, Acta Biomater. 177 (2024) 1–19.

[37] H.-R. Jia, Y.-X. Zhu, Z. Chen, F.-G. Wu, Cholesterol-assisted bacterial cell surface engineering for photodynamic inactivation of gram-positive and gram-negative bacteria, *ACS Appl. Mater. Interfaces* 9 (19) (2017) 15943–15951.

[38] Z. Zhao, X. Shan, H. Zhang, X. Shi, P. Huang, J. Sun, Z. He, C. Luo, S. Zhang, Nitric oxide-driven nanotherapeutics for cancer treatment, J. Control. Release 362 (2023) 151–169.

[39] N. Li, N. Li, Q. Yi, K. Luo, C. Guo, D. Pan, Z. Gu, Amphiphilic peptide dendritic copolymer-doxorubicin nanoscale conjugate self-assembled to enzyme-responsive anti-cancer agent, Biomaterials 35 (35) (2014) 9529–9545.

[40] N. Li, H. Cai, L. Jiang, J. Hu, A. Bains, J. Hu, Q. Gong, K. Luo, Z. Gu, Enzyme-sensitive and amphiphilic PEGylated dendrimer-paclitaxel prodrug-based nanoparticles for enhanced stability and anticancer efficacy, ACS Appl. Mater. Interfaces 9 (8) (2017) 6865–6877.

[41] X. Song, H. Cai, Z. Shi, Z. Li, X. Zheng, K. Yang, Q. Gong, Z. Gu, J. Hu, K. Luo, Enzyme-responsive branched glycopolymer-based nanoassembly for co-delivery of paclitaxel and akt inhibitor toward synergistic therapy of gastric cancer, Adv. Sci. 11 (2) (2024) e2306230.

[42] X. Li, Z. Duan, Z. Li, L. Gu, Y. Li, Q. Gong, Z. Gu, K. Luo, Dendritic polymer-functionalized nanomedicine potentiates immunotherapy *via* lethal energy crisis-induced PD-L1 degradation, Biomaterials 302 (2023) 122294.

[43] Y. Jin, J. Fan, R. Wang, X. Wang, N. Li, Q. You, Z. Jiang, Ligation to scavenging strategy enables on-demand termination of targeted protein degradation, J. Am. Chem. Soc. 145 (13) (2023) 7218–7229.

[44] J. Zhu, J. Tian, C. Yang, J. Chen, L. Wu, M. Fan, X. Cai, L-arg-rich amphiphilic dendritic peptide as a versatile NO donor for NO/photodynamic synergistic treatment of bacterial infections and promoting wound healing, Small 17 (32) (2021) e2101495.

[45] J. Chen, D. Zhu, B. Lian, K. Shi, P. Chen, Y. Li, W. Lin, L. Ding, Q. Long, Y. Wang, E. Laurini, W. Lan, Y. Li, A. Tintaru, C. Ju, C. Zhang, S. Pricl, J. Iovanna, X. Liu, L. Peng, Cargo-selective and adaptive delivery of nucleic acid therapeutics by bola-amphiphilic dendrimers, Proc. Natl. Acad. Sci. 120 (21) (2023) e2220787120.

[46] X. Zhou, B. Zhao, L. Wang, L. Yang, H. Chen, W. Chen, H. Qiao, H. Qian, A glucose-responsive nitric oxide release hydrogel for infected diabetic wounds treatment, J. Control. Release 359 (2023) 147–160.

[47] D.-W. Zheng, Y. Chen, Z.-H. Li, L. Xu, C.-X. Li, B. Li, J.-X. Fan, S.-X. Cheng, X.-Z. Zhang, Optically-controlled bacterial metabolite for cancer therapy, Nat. Commun. 9 (1) (2018) 1680.

[48] W. Fan, N. Lu, P. Huang, Y. Liu, Z. Yang, S. Wang, G. Yu, Y. Liu, J. Hu, Q. He, J. Qu, T. Wang, X. Chen, Glucose-responsive sequential generation of hydrogen peroxide and nitric oxide for synergistic cancer starving-like/gas therapy, Angew. Chem. Int. Edit. 56 (5) (2016) 1229–1233.

[49] J. Jia, W. Chen, L. Xu, X. Wang, M. Li, B. Wang, X. Huang, T. Wang, Y. Chen, M. Li, D. Tian, J. Zhuang, X. Lin, N. Li, Codelivery of dihydroartemisinin and chlorin e6 by copolymer nanoparticles enables boosting photodynamic therapy of breast cancer with low-power irradiation, Regen. Biomater. 10 (2023) rbad048.

[50] L. Jiang, D. Chen, Z. Jin, C. Xia, Q. Xu, M. Fan, Y. Dai, J. Liu, Y. Li, Q. He, Light-triggered nitric oxide release and structure transformation of peptide for enhanced intratumoral retention and sensitized photodynamic therapy, Bioact. Mater. 12 (2022) 303–313.

[51] Y. Yu, R. Tian, Y. Zhao, X. Qin, L. Hu, J.J. Zou, Y.W. Yang, J. Tian, Self-assembled corrole/chitosan photothermal nanoparticles for accelerating infected diabetic wound healing, Adv. Healthc. Mater. 12 (16) (2023) e2201651.

[52] V. Saluja, Y. Mishra, V. Mishra, N. Giri, P. Nayak, Dendrimers based cancer nanotheranostics: an overview, Int. J. Pharmacol. 600 (2021) 120485.

[53] S. Zhu, Q. Dai, L. Yao, Z. Wang, Z. He, M. Li, H. Wang, Q. Li, H. Gao, X. Cao, Engineered multifunctional nanocomposite hydrogel dressing to promote vascularization and anti-inflammation by sustained releasing of Mg^{2+} for diabetic wounds, Compos. Part b: Eng. 231 (2022) 109569.

[54] W. Zhang, Y. Zhou, Y. Fan, R. Cao, Y. Xu, Z. Weng, J. Ye, C. He, Y. Zhu, X. Wang, Metal-organic-framework-based hydrogen-release platform for multieffective helicobacter pylori targeting therapy and intestinal flora protective capabilities, Adv. Mater. 34 (2) (2022) e2105738.

[55] W. Liu, R. Gao, C. Yang, Z. Feng, W. Ou-Yang, X. Pan, P. Huang, C. Zhang, D. Kong, W. Wang, ECM-mimetic immunomodulatory hydrogel for methicillin-resistant staphylococcus aureus-infected chronic skin wound healing, Sci. Adv. 8 (27) (2022) eabn7006.

[56] M. Kharaziha, A. Baidya, N. Annabi, Rational design of immunomodulatory hydrogels for chronic wound healing, Adv. Mater. 33 (39) (2021) e2100176.